

# Symmetry and scale orient Min protein patterns in shaped bacterial sculptures

Fabai Wu, Bas G. C. van Schie, Juan E. Keymer<sup>†</sup> and Cees Dekker<sup>\*</sup>

**The boundary of a cell defines the shape and scale of its subcellular organization. However, the effects of the cell's spatial boundaries as well as the geometry sensing and scale adaptation of intracellular molecular networks remain largely unexplored. Here, we show that living bacterial cells can be 'sculpted' into defined shapes, such as squares and rectangles, which are used to explore the spatial adaptation of Min proteins that oscillate pole-to-pole in rod-shaped *Escherichia coli* to assist cell division. In a wide geometric parameter space, ranging from  $2 \times 1 \times 1$  to  $11 \times 6 \times 1 \mu\text{m}^3$ , Min proteins exhibit versatile oscillation patterns, sustaining rotational, longitudinal, diagonal, stripe and even transversal modes. These patterns are found to directly capture the symmetry and scale of the cell boundary, and the Min concentration gradients scale with the cell size within a characteristic length range of 3–6  $\mu\text{m}$ . Numerical simulations reveal that local microscopic Turing kinetics of Min proteins can yield global symmetry selection, gradient scaling and an adaptive range, when and only when facilitated by the three-dimensional confinement of the cell boundary. These findings cannot be explained by previous geometry-sensing models based on the longest distance, membrane area or curvature, and reveal that spatial boundaries can facilitate simple molecular interactions to result in far more versatile functions than previously understood.**

Pattern formation is central to the wealth of nature's intrigue. In search for its origin, Alan Turing theoretically showed that the simple reaction and diffusion of two chemicals is adequate to spontaneously form reproducible spatial patterns<sup>1</sup>. Reaction–diffusion theory subsequently inspired broad applications in physics and chemistry and bridged molecular interactions to morphogenesis and cellular organization in biology<sup>1–8</sup>. Reaction–diffusion systems are, however, little understood in the context of a boundary geometry, which is of particular importance in embryos and cells, where spatial patterns such as protein gradients are established within their envelope to dictate the locations for fundamental cellular processes such as cell division<sup>5,9–11</sup>. In this study, we demonstrate how reaction–diffusion patterns of Min proteins can sense and adapt to the morphological features of bacterial cells, an ability that is essential for spatial regulation for cell division and its robustness against variations in cell size and shape<sup>12–14</sup>.

Min proteins in many bacteria, including rod-shaped *Escherichia coli*, exhibit a fascinating phenomenon: they oscillate pole-to-pole along the cell length, resulting in a time-averaged concentration minimum of division inhibitors at the mid-plane<sup>10,11</sup> (Fig. 1b). This oscillatory dynamics is believed to arise autonomously from the ability of MinD proteins to cooperatively bind to the cytoplasmic membrane and the ability of MinE proteins to unbind MinD from the membrane<sup>15,16</sup> (Fig. 1a), actions that, respectively, exemplify the self-activation and inhibition kinetics of reaction–diffusion theory<sup>3,4,7</sup>. The self-organizing nature of dynamic Min patterns has been elegantly demonstrated by travelling waves and oscillations reconstituted *in vitro*<sup>17–21</sup>, albeit exhibiting an approximately tenfold larger length scale compared to Min oscillations *in vivo* due to factors that remain unclear.

Various spatial cues have been hypothesized to account for the consistent pole-to-pole orientation of the Min oscillations<sup>7,18,19,22–24</sup>, including the longest travel distance through the cytosol<sup>22</sup> or along the membrane<sup>19</sup>, a characteristic polar membrane area<sup>18</sup> and

a high membrane curvature at the poles<sup>24</sup> (Fig. 1c). Furthermore, it is unclear how Min gradients quantitatively adapt to cell size variability and growth. Here, we identify the rules of geometry sensing and scale adaptation by systematically studying the dynamic behaviour of Min proteins in live cells within spatial boundaries across a broad geometric parameter space.

## Bacterial cells can be sculpted into defined shapes

Bacteria maintain their cell shape by a well-regulated process of peptidoglycan insertion into the cell wall<sup>25</sup>. Previous studies have shown that curved agarose micro-chambers can alter the growth of filamentous cells of *E. coli* such that they adopt a certain degree of curvature<sup>26</sup>, and that sub-micrometre constraints imposed by silicon slits can induce *E. coli* to grow into a variety of squeezed shapes<sup>27</sup>. These methods have been applied to elucidate interesting mechanisms of growth and division in bacteria<sup>13,28</sup>. The diversity and reproducibility of the cell shapes produced by these methods are, however, limited, as wild-type pathways for cell wall synthesis are used. Spheroplasts generated by lysozyme, on the other hand, appear to abolish the dynamic activities of proteins such as Min oscillations<sup>24</sup>.

For this study, we developed a new 'cell-sculpting' method to shape living bacterial cells into user-defined geometries (Fig. 1d). This allowed a quantitative and systematic study on the effect of shape and scale. Cells were inoculated into nanofabricated polydimethylsiloxane (PDMS) chambers with various lateral shapes and a fixed depth of  $1.15 \pm 0.05 \mu\text{m}$  (Supplementary Fig. 1). The 10- $\mu\text{m}$ -thick layer of PDMS was supported by a thin cover glass for microscopy, and the microchambers with cells were covered by a 5% agarose pad supplemented with growth medium, A22 and cephalaxin. A22 inhibits rod-shape maintenance by antagonizing the dynamics of bacterial actin MreB, which regulates peptidoglycan insertion patterns. Cephalaxin prevents the cell wall constriction that would otherwise lead to cell division. Under these growth conditions, *E. coli* cells exhibit a surprising plasticity, growing into

Department of Bionanoscience, Kavli Institute of Nanoscience, Delft University of Technology, Lorentzweg 1, Delft 2628 CJ, The Netherlands. <sup>†</sup>Present address: IEB & Department of Ecology, School of Biological Sciences, P. Catholic University, Casilla 114-D, Santiago, Chile. \*e-mail: c.dekker@tudelft.nl

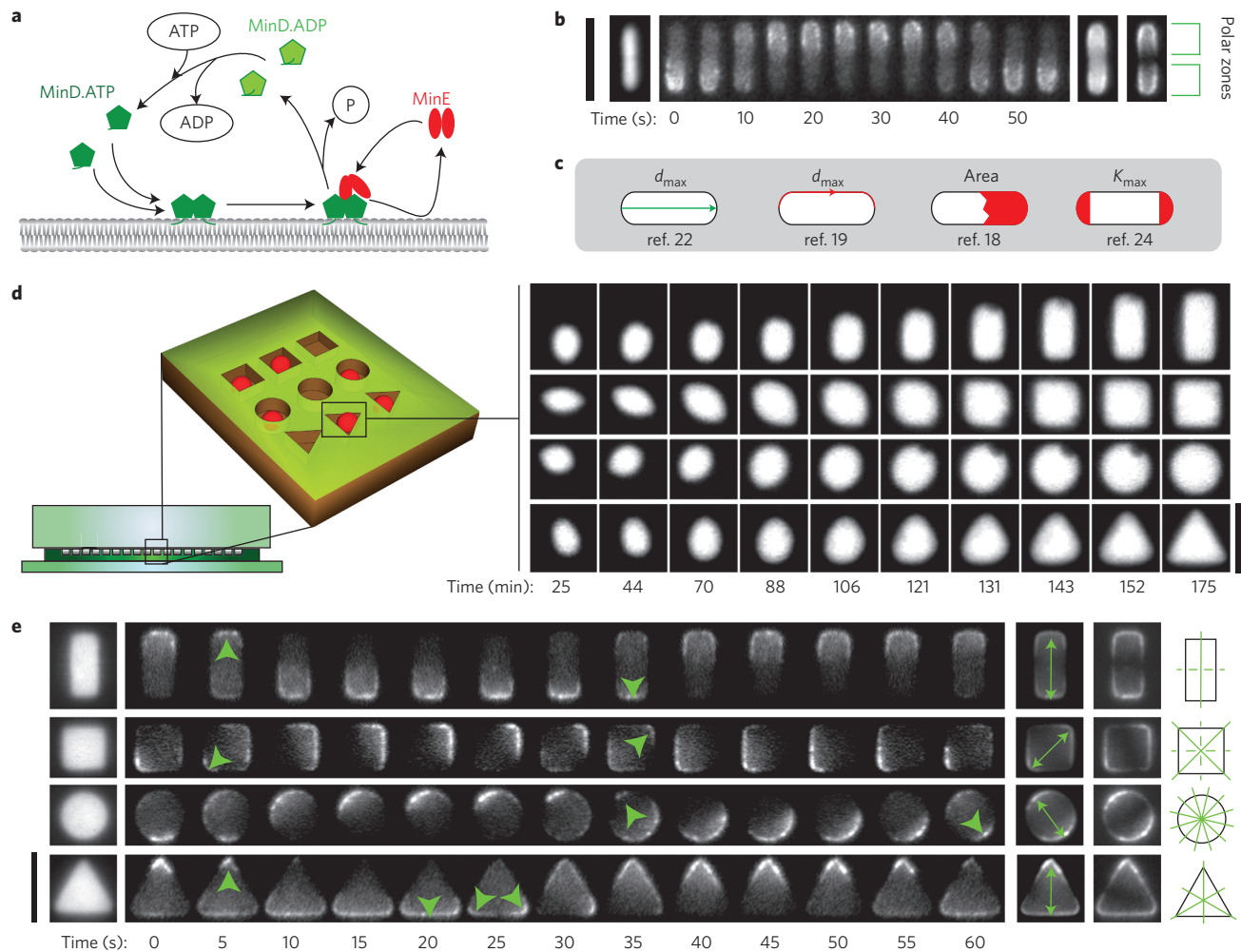


**Figure 1 | Min proteins oscillate along the symmetry axes of *E. coli* shaped by the 'cell-sculpting' technique.** **a**, Schematic of interactions between Min proteins and the membrane. P, phosphate; ATP, adenosine triphosphate; ADP, adenosine diphosphate. **b**, Left to right: fluorescence images of cytosolic eqFP670, sFGFP-MinD time series, time-averaged intensity and standard deviation (s.d.) of the sFGFP-MinD in rod-shaped *E. coli*. **c**, Previous geometry-sensing models from the given references. Green, cytosolic distance; red, membrane distance (line) and area (shaded); **d**, distance;  $K$ , curvature. **d**, Left: schematic of the cell-sculpting device, composed of a microscope coverglass (bottom), PDMS micro-chambers (middle) and an agarose pad supplemented with nutrient and drugs (top). Right: cytosolic eqFP670 fluorescence images of cells growing into defined shapes. **e**, Image sequence as in **b**, followed by illustrations of symmetry axes. Green arrows indicate cell poles defined by the Min patterns. Solid lines, long axes; dashed lines, short axes. Scale bars in **b,d,e**, 5  $\mu\text{m}$ .

cell volumes more than 20 times larger than a regular cell. During several hours of growth, the cells gradually adapted their shapes to the chambers with defined lateral geometries (circles, squares, rectangles and triangles; Fig. 1d and Supplementary Movie 1). These cells generally maintained their defined shape for 10–20 min (during which time we captured the Min oscillations) before they grew out of the chamber (Supplementary Fig. 2). For statistical analysis, many tens of cells (6–118 cells, Supplementary Table 1) were selected for each geometric parameter, to give a total data set comprising 2,268 qualified cells.

### Min oscillations in diverse shapes

To visualize Min protein dynamics, we inserted a green fluorescent protein fusion gene (*sfGFP-minD*) at the endogenous *minD* genomic locus (Supplementary Methods and Supplementary Tables 2 and 3). This is the first reported endogenous fusion that rescues the MinD deletion phenotype and retains the wild-type MinD protein level, growth rate and cell morphology (Supplementary Figs 3 and 4 and Supplementary Movie 2). The total fluorescence intensity of sfGFP-MinD scales linearly with cell size, indicating that the MinD concentration is roughly constant during growth

(Supplementary Fig. 5). The dynamic localizations of the MinD proteins in cells were typically recorded with an interval of 5 s for a period of 2 min, and are presented as the standard deviation (s.d.) of fluorescence intensity over time calculated per pixel (Fig. 1e).

Remarkably, the Min proteins were found to sustain oscillation patterns in a wide range of cell shapes and sizes (Fig. 1e and Supplementary Movie 3), including shapes that deviate strongly from the wild-type rod shape and that possess multiple symmetry axes and highly curved regions, such as rectangles, squares, circles and equilateral triangles. As shown in Fig. 1e, Min oscillations are found to align to the longitudinal axis in a  $2 \times 4.5 \mu\text{m}^2$  rectangle, but, in contrast, in a square of 3  $\mu\text{m}$ , they can occur between diagonal corners. In a circle with a diameter of 3.4  $\mu\text{m}$ , MinD proteins toggle between opposing ends of its diameter, while in an equilateral triangle (side lengths 4.5  $\mu\text{m}$ ), they oscillate between one corner and its opposite side. These patterns reveal that the Min proteins preferably oscillate along one of the symmetry axes (see also Supplementary Fig. 6 for a longer timescale).

### Symmetry and scale orient Min protein patterns

When exploring the same cell shape but different lateral sizes, Min proteins can display qualitatively different dynamic patterns

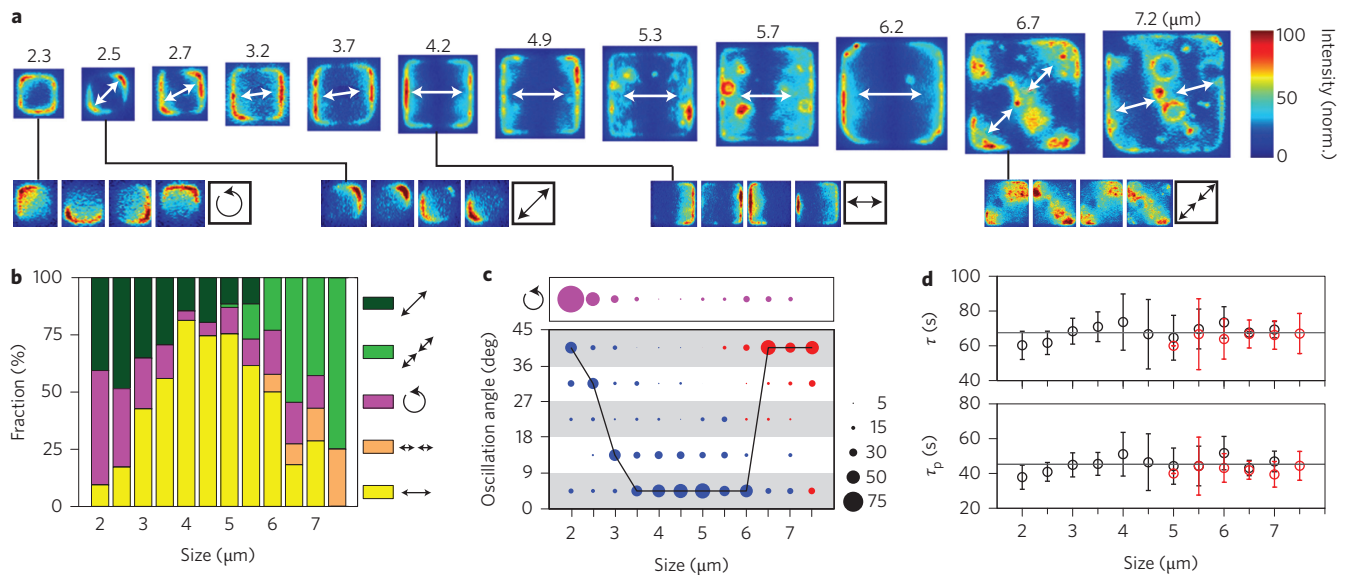


**Figure 2 | A characteristic range dictates the Min oscillation axis choice.** **a**, Standard deviation (s.d.) patterns of sfGFP-MinD oscillations in cells with sizes as indicated. Insets at the bottom are time-lapse montages and schematics of the modes of oscillations. **b**, Bar diagram illustrating the relative occurrence of each mode of oscillation as a function of cell size. **c**, Ball plot illustrating the dependence of oscillation angle on cell size. Angles are confined to the range 0–45° due to symmetry. Ball diameter represents the percentage of cells at a certain size. The rotational mode (magenta) is excluded in these percentages and is plotted above, normalized against all cells showing pole-to-pole (blue) or stripe (red) patterns. **d**, Period  $\tau$  and polar residence time  $\tau_p$  of the Min oscillations as a function of cell size. Black symbols, pole-to-pole oscillations; red symbols, stripe patterns; grey lines, mean values for all data. Error bars denote s.d. In **b–d**, sizes represent side lengths.

(Fig. 2). As the size (side lengths) of squares increases from 2  $\mu\text{m}$  to as large as 7.5  $\mu\text{m}$ , Min patterns undergo transitions from rotational motions along the lateral periphery, to diagonal pole-to-pole oscillations, to side-to-side oscillations and then to three-node stripe patterns along the diagonals (Fig. 2a,b and Supplementary Movie 4). At the transition points, the major angles of oscillations switch steeply between near 0° and near 45° (Fig. 2c), reflecting a strong tendency of the oscillations to align to the symmetry axes of the square shape. Note that the observed variety of patterns cannot be explained by the longest-distance or high-curvature rules that have been proposed to explain Min patterns<sup>19,22,24</sup>.

The side-to-side oscillation mode dominates the pattern distribution in the sampled size range (Fig. 2b). Its occurrence as a function of cell size resembles a normal distribution, with a mean pole-to-pole distance of 4.6  $\mu\text{m}$  and a full-width at half-maximum value of 3.2  $\mu\text{m}$ , spanning a large range of 3.0–6.2  $\mu\text{m}$  (yellow bars in Fig. 2b). Rotational motions occur predominantly in cells around 2  $\mu\text{m}$ , where all cell dimensions are below 3  $\mu\text{m}$ , indicating that the lower bound of the characteristic range (3  $\mu\text{m}$ ) approximates the smallest length scale for Min proteins to sustain robust oscillatory dynamics<sup>29</sup>. Diagonal pole-to-pole oscillations are shown most frequently in cells around 2.5  $\mu\text{m}$ , that is, with diagonal lengths of 3–4  $\mu\text{m}$ . The stripe patterns start to emerge as the cells' diagonals exceed 6  $\mu\text{m}$ , and dominate when the cell widths exceed 6.25  $\mu\text{m}$ , the upper bound of the characteristic range (Supplementary Fig. 7). All these observations indicate that the axis choice in square-shaped cells is dictated by a characteristic length range of 3–6  $\mu\text{m}$ .

The temporal scale of the Min oscillations is surprisingly constant, with period ( $68 \pm 13$  s, mean  $\pm$  s.d.) and polar residence time ( $45 \pm 11$  s) that are rather insensitive to large increases in cell size or differences in the mode of oscillations (Fig. 2d and Supplementary Figs 8, 9). This demonstrates that the spatial properties of the Min patterns can be regulated independently of the temporal properties.

### Versatile adaptation, transversal mode and heterogeneity

To explore the effects of symmetry selection and the characteristic length range on the robustness and versatility of the Min patterns, we sampled the Min patterns in rectangular cells with dimensions ranging from  $2 \times 1 \times 1$  to  $11 \times 6 \times 1 \mu\text{m}^3$  (Fig. 3a, Supplementary Fig. 10 and Supplementary Movies 5–7). Seven modes of Min patterns emerged in this geometric parameter space (Fig. 3b), including a striking transversal mode that finds the shortest lateral distance in cells with widths of 3.5–6.5  $\mu\text{m}$ , and ‘zigzag’ patterns that exploit an even longer path than the cell’s diagonal. As can be seen from the phase diagrams in Fig. 3c,d, the longitudinal modes appear to be the majority pattern, with transversal modes dominating in wider cells. Rotational, diagonal and zigzag patterns occur at the interfaces between the spatial regimes for the major patterns, suggesting that they are less robust states that take place at the transitions between major patterns (Fig. 3c). For cells below 2.5  $\mu\text{m}$  in length, Min proteins mostly exhibit stochastic fluctuations rather than stable oscillations, similar to those observed in a previous report<sup>29</sup> (Supplementary Fig. 11).

The accuracy of symmetry alignment and the consistency of axis choice are determined by the cell dimensions and the number of symmetry axes of a given cell shape, as can be illustrated by comparing the Min patterns in squares and rectangles (Figs 3a,c–e and 4a). Whereas a square has four symmetry axes, a slight increase in aspect ratio (AR) deforms it to a rectangle, immediately removing the diagonals as symmetry axes and leaving only one long axis and one short axis. Indeed, a small increase in AR from unity drastically decreases the Min oscillation angle, which approaches the longitudinal symmetry axis with a decay constant of 0.13 (Fig. 3b shows data for cells 2.25–3.25  $\mu\text{m}$  wide). The increase in AR dramatically enhances the consistency of the oscillation angle, from  $37 \pm 27^\circ$  for  $\text{AR} < 1.05$ , reflecting the occurrence of both longitudinal and diagonal patterns, to  $1.7 \pm 2.7^\circ$  for  $\text{AR} = 2.00 \pm 0.25$ , with exclusively longitudinal oscillations. Such a consistent alignment to the long axis is, however, jeopardized when the short axis (cell width) increases to sizes greater than 3.5  $\mu\text{m}$ , where the transversal mode

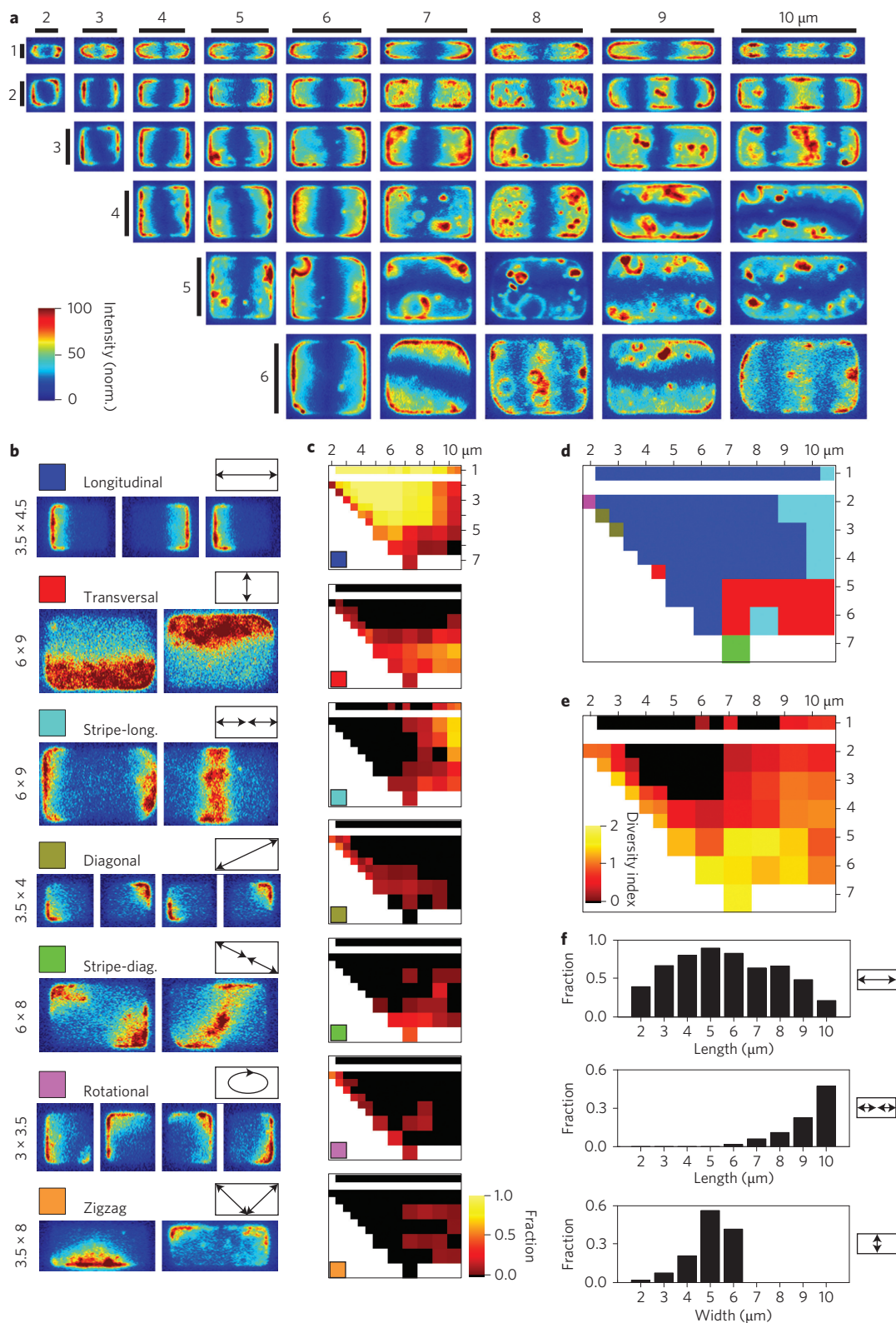


**Figure 3 | Robustness and variation of Min patterns in a wide geometric parameter space.** **a**, Representative Min s.d. patterns in rectangular cells. **b**, Time-lapse images of representative examples of the seven oscillation modes. Each mode is presented with a colour box representing this mode in **b** and **c**, a time montage, and a schematic. **c**, Phase diagrams depicting the fraction of individual modes occurring in each rectangle size. Percentage denotes the fraction of cells with this mode, relative to the total number of cells at this rectangle size. White areas depict unsampled geometry. Lateral dimensions are indicated in micrometres and scaled as in **a**. **d**, Phase diagram showing the distribution of the seven modes mapping the patterns that exhibit maximum occupancy for each cell dimension. Colours represent different modes, as indicated in **b** and **c**. **e**, Phase diagram showing the heterogeneity of oscillation patterns for each rectangle size. **f**, Bar plots presenting the fractions of rectangular cells for a given length or width that show the first three major modes, respectively.

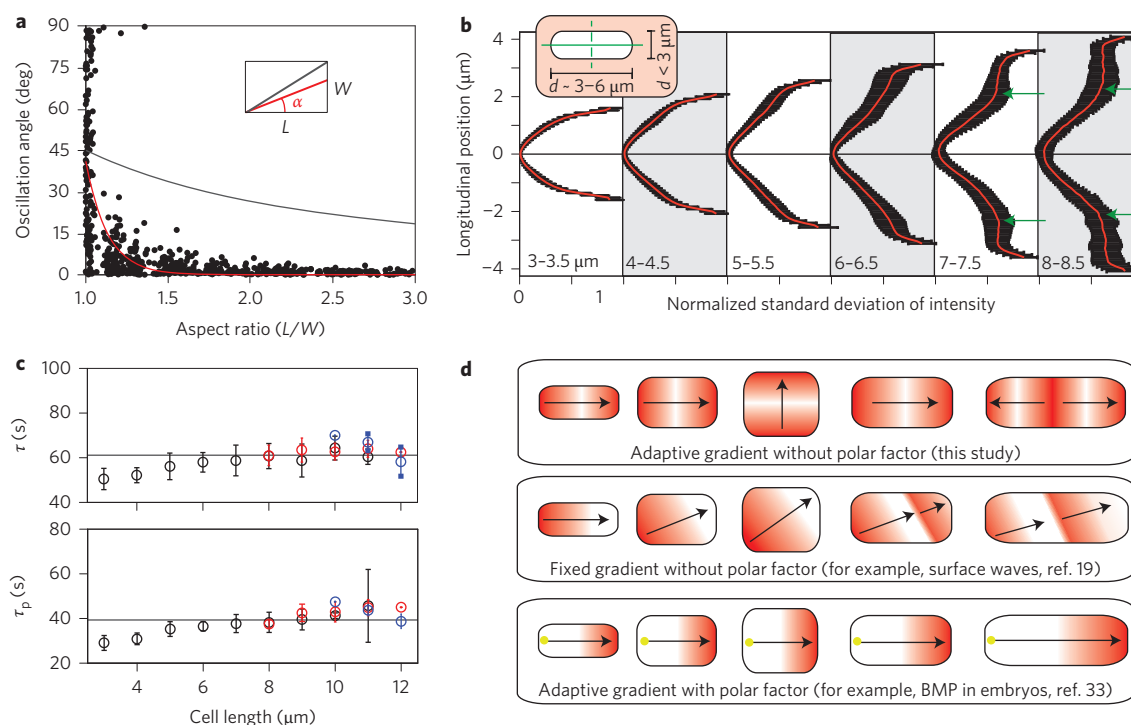


**Figure 4 | Symmetry selection, gradient scaling and adaptive range in Min patterns.** **a**, Oscillation angle  $\alpha$  versus aspect ratio in rectangular cells with widths of 2.25–3.5  $\mu\text{m}$ . Grey line, diagonal angles; red line, exponential fit. **b**, sFGFP-MinD s.d. intensity profiles along the long axes of cells with lengths of 3–8.5  $\mu\text{m}$  and widths of 2–3.25  $\mu\text{m}$ . Red lines, mean profile; black error bars, s.d.; green arrows, start of the polar plateau. All horizontal axes share the label indicated on the left. Cell lengths are given at the bottom. Inset: the demands for robust longitudinal pole-to-pole oscillations. **c**, Period  $\tau$  and polar residence time  $\tau_p$  of the Min oscillations as a function of cell length in rectangular cells with widths of 2.25–2.75  $\mu\text{m}$ . Black symbols, pole-to-pole oscillations; red symbols, three-node stripe patterns; blue symbols, three-node stripe patterns; grey lines, mean values for all data. Error bars denote s.d. **d**, Illustrations of patterns in a variety of rectangles for three different types of gradient formation. Red, high concentration; white, low concentration; black arrow, protein travel direction; yellow dots, inhibitor source.

emerges to coexist with the longitudinal modes (Fig. 3b–f). The requirement of a symmetry axis for stable Min oscillations also explains our previous observation that strongly non-symmetric cells yield fluctuating Min patterns<sup>13</sup>.

We evaluated the heterogeneity of the Min patterns by scoring the Shannon entropy (a diversity index measure)<sup>30</sup> of the oscillation modes for each cell size (Fig. 3e). The coexistence of patterns is not only apparent for the squares, but is also evident for large cell dimensions. For example, of all the  $2 \times 9 \mu\text{m}$  cells, 15 cells (48%) oscillate pole-to-pole, and 16 cells (52%) show a three-node stripe mode. In cells longer than 10  $\mu\text{m}$ , the pole-to-pole mode vanishes and four-node stripes begin to emerge (Supplementary Movie 8). Also, despite the observation that the transversal mode dominates for larger cell widths, it is not the exclusive pattern observed for any of these cell sizes. These are interesting multi-stability phenomena that are yet to be explored by pattern-formation theories.

### Gradient scaling, adaptive range and temporal stability

The longitudinal pole-to-pole oscillations are the majority mode in rectangular cells with a length of 3–8  $\mu\text{m}$  and a width below 4  $\mu\text{m}$  (Fig. 3d). Despite the significant variation in cell length, the s.d. and time-averaged intensity profiles for these cells consistently indicate a high polar residence of MinD and minima that are located at mid-cell with an average deviation of only 2.6% relative to the cell length (Fig. 4b and Supplementary Fig. 12). This is consistent with the remarkable accuracy with which wild-type *E. coli* divide at the middle of cells with variable cell lengths<sup>13,31</sup>.

Cells of 3–6  $\mu\text{m}$  in length exhibit s.d. MinD profiles and time-averaged MinD profiles that scale surprisingly well with cell length (Fig. 4b and Supplementary Fig. 12), which is not expected

from a scenario where a fixed Min wavelength would determine the gradient. MinD-binding zones are observed to always initiate at the extremities of the longitudinal axes in these cells. When cells grow longer, MinD proteins often first establish binding zones away from the poles, resulting in broad plateaux at the two ends of the s.d. intensity profiles that no longer scale with length. The establishment of MinD binding zones away from the cell poles can eventually lead to the formation of a middle stripe, as observed in the stripe patterns (Supplementary Fig. 13). Indeed, transitions from pole-to-pole into a stripe mode can occur throughout cell lengths between 7 and 11  $\mu\text{m}$  (Fig. 3e), which is probably subject to stochasticity<sup>32</sup>.

In 2  $\mu\text{m}$  wide cells with a length spanning a large range of 3–12  $\mu\text{m}$ , the oscillation period and polar residence time of Min proteins are found to be about constant, with only a small degree of variation (Fig. 4c). Similar to square shapes, these temporal scales are not affected by the number of nodes in the oscillations (Fig. 4c and Supplementary Movie 8). With a stabilized temperature of  $27.0 \pm 0.3 \text{ }^\circ\text{C}$ , the standard deviation of the period is typically about 5 s (Fig. 4c). Note that the insensitivity of the temporal scale to cell length that we quantified here *in vivo* is qualitatively different from the constant velocity of *in vitro* Turing waves that are unconfined<sup>17</sup>. The fact that the period of *in vivo* Min oscillations does not scale with cell size can be understood from the fact that the establishment of the MinD polar zone is not constrained by diffusion, but by MinE sequestration<sup>4,7</sup> (Supplementary Fig. 13c). While a larger MinD polar zone attracts more MinD due to cooperative membrane binding, it simultaneously enhances MinE binding and thus increases the tendency to ‘push’ MinD to the other pole.

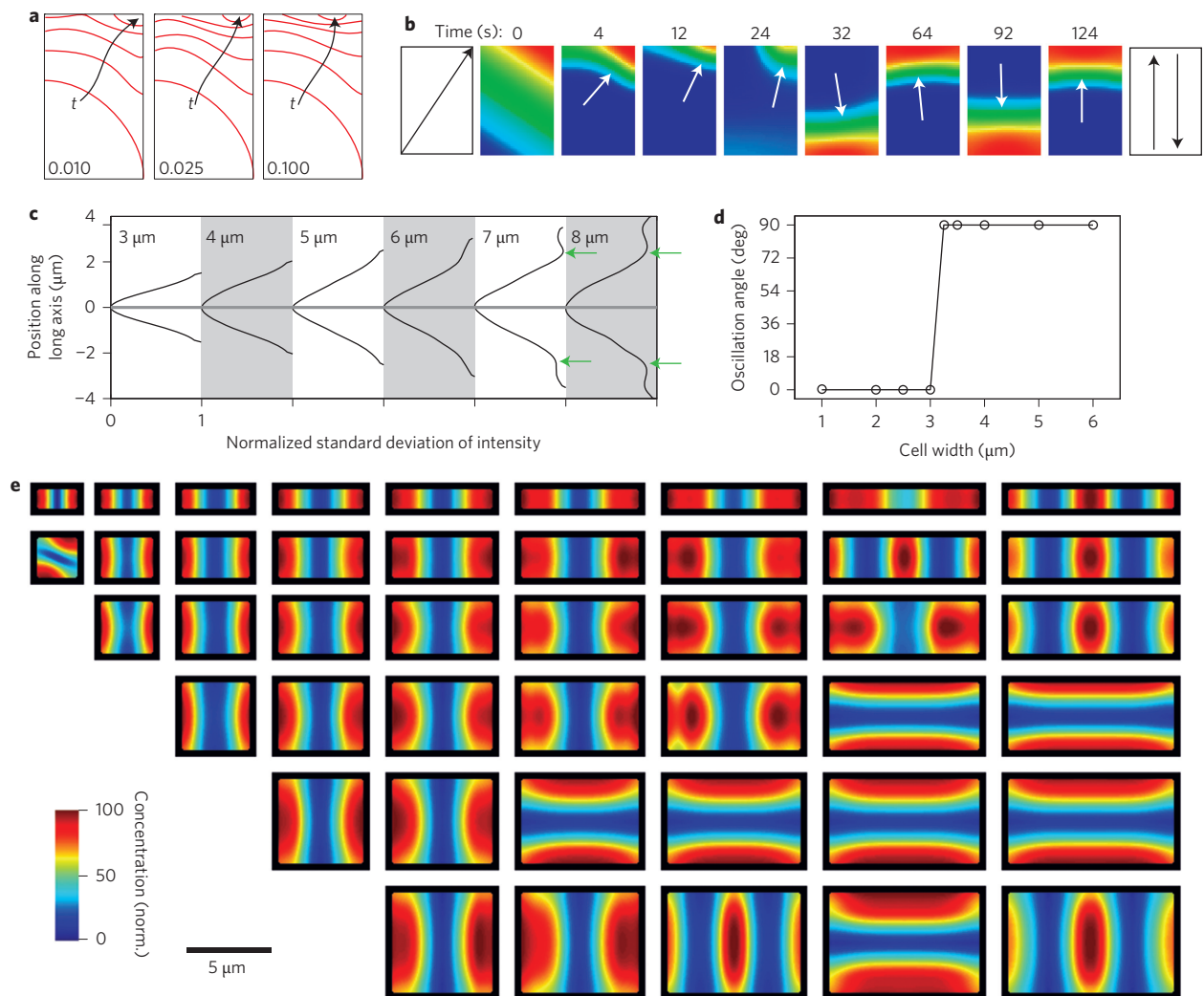


**Figure 5 | Numerical simulations of a three-dimensional reaction-diffusion model explain the sensing of symmetry and scale by Min proteins.**

**a**, Schematics showing the movement of MinD polar zones (contours denoted by red lines, direction by black arrows) over time for different values of  $k_{dD}$  (denoted at the bottom, units of  $\mu\text{m}^2 \text{s}^{-1}$ ) in  $5 \times 3 \times 1 \mu\text{m}^3$  cells. **b**, An initially diagonal MinD gradient in a  $3 \times 2 \times 1 \mu\text{m}^3$  cell develops into longitudinal pole-to-pole oscillations. **c**, S.d. profiles of MinD concentration in 2- $\mu\text{m}$ -wide cells with various lengths (indicated at the top). Green arrow, start of polar plateau. **d**, Oscillation angle (indicating longitudinal versus transversal oscillations) as a function of cell width. **e**, S.d. images of the two-dimensional projection of MinD concentrations from the three-dimensional simulations at 480–600 s.

What underlies the symmetry alignment and adaptive scaling of the Min protein patterns? These features have not been examined in previous Turing-type models, which generally exhibit a fixed wavelength<sup>1–3,6,17,19</sup>. To achieve symmetry alignment, spatial confinement seems required, as *in vitro* Min surface waves travel along the diagonals of rectangular lipid patches<sup>19</sup>, and are apparently insensitive to the symmetry axes (Fig. 4d, middle panel). Interestingly, recent *in vitro* work on Min proteins in partly confined microwells also showed transversal oscillations<sup>20</sup>, although with a different length scale and with different pattern dynamics compared to the *in vivo* behaviour observed here. The adaptive range could potentially be assisted by extra chemical or mechanical cues<sup>18,24</sup>, but such scenarios do not fit our data quantitatively (Supplementary Discussion and Supplementary Fig. 14). Mechanisms proposed for pattern scaling in developing embryos rely on production-degradation feedbacks, active transport of morphogen ligands by a polarized source of inhibitors (Fig. 4d, bottom panel) or the physiological state of cells in tissues, which do not apply to our intracellular scenario<sup>33–36</sup>. With current explanations lacking, we thus ask whether symmetry alignment

and adaptive scaling are features that are yet to be uncovered from the Min reaction–diffusion mechanism.

### Simulations capture symmetry and gradient scaling

Using numerical simulations, we now show that a kinetic parameter regime can be found for the Min reaction–diffusion system that leads to both symmetry alignment and gradient scaling, when and only when Min proteins are confined to a three-dimensional geometry (Fig. 5a–d). Strikingly, this allows all the major patterns observed in our experiments (Fig. 3a) to be stabilized over the full range of cell sizes in deterministic simulations using one fixed set of kinetic parameters (Fig. 5e and Supplementary Movie 9). The model also shows that the period of Min oscillations is rather insensitive to variations in cell length within the measured range (Supplementary Movie 9 and Supplementary Fig. 15).

To probe for the above-highlighted geometry-sensing properties, we carried out a parameter screening of all reaction rates within a model containing a minimal set of self-activation/inhibition interactions between Min proteins<sup>32</sup> (shown in Fig. 1a). This model uses the rate at which membrane-bound MinD proteins recruit

cytosolic MinD to constrain the strength of polar-zone binding, a finite ADP-ATP nucleotide exchange rate of MinD to delay reattachment<sup>4</sup> and sequestering of the polar MinD by MinE that allows the detached MinD to escape and reattach to the membrane at a distance<sup>7,37</sup>. Parameter constraints for this model that led to robust oscillatory behaviour were previously determined by Halatek and Frey using two-dimensional elliptic geometries<sup>7</sup>.

To explore the microscopic origin of the symmetry selection, we carried out simulations starting from an asymmetric MinD polar zone (Fig. 5a and Supplementary Movie 10). We found that the orientation of polar zone development is most affected by the MinD self-recruitment rate ( $k_{\text{dD}}$ ). With a sufficiently high  $k_{\text{dD}}$ , an initial diagonal MinD gradient (for example, in a  $3 \times 2 \times 1 \mu\text{m}^3$  rectangle) is found to rapidly align to the longitudinal axis within a few pole-to-pole oscillation cycles (Fig. 5b, Supplementary Fig. 16 and Supplementary Movies 11 and 12), whereas lowering the  $k_{\text{dD}}$  leads to a higher stability for diagonal, non-symmetric oscillations in this rectangular shape (Supplementary Fig. 16). Importantly, symmetry selection is only achieved through oscillations in a three-dimensionally confined volume, thus explaining the lack of symmetry in unconfined two-dimensional surface waves<sup>19</sup>.

Gradient scaling of longitudinal oscillations in 3- to 6- $\mu\text{m}$ -long cells is determined by multiple kinetic parameters (including  $k_{\text{dD}} = 0.05 \mu\text{m}^2 \text{s}^{-1}$ ). Importantly, fitting the 3–6  $\mu\text{m}$  scaling range simultaneously yields transversal oscillations in cells wider than 3  $\mu\text{m}$  and sustainable longitudinal stripes in cells longer than 6  $\mu\text{m}$  (Fig. 5c,d). The presence of a finite scaling range requires  $k_{\text{dD}}$  to be within a quite narrow window of 0.03–0.10  $\mu\text{m}^2 \text{s}^{-1}$ . For  $k_{\text{dD}} < 0.03 \mu\text{m}^2 \text{s}^{-1}$ , polar plateaux do not appear in the s.d. gradients for cells of any lengths, whereas for  $k_{\text{dD}} > 0.10 \mu\text{m}^2 \text{s}^{-1}$ , the gradients do not scale. A previous theoretical suggestion<sup>7</sup> that transitions from pole-to-pole into stripes are not robust for  $k_{\text{dD}}$  below 0.10  $\mu\text{m}^2 \text{s}^{-1}$  is in line with our experimental observation of a variable length (7–11  $\mu\text{m}$ ) where such transitions happen (Fig. 3f). Altogether, the analyses indicate that transitions between oscillation modes are intrinsically coupled to the scaling property of the concentration gradients. In future work, our deterministic simulations can be extended to analyse the robustness and heterogeneity of patterns against internal and external fluctuations<sup>32,38</sup> and to unravel the role of more detailed molecular interactions such as a conformational switch and membrane binding of MinE<sup>39,40</sup>.

## Conclusions

Taken together, the key mechanism revealed by our experiments is that Min proteins orient their oscillation patterns by sensing both the symmetry and scale of the cellular geometry. We find that Min proteins explore cellular space to select the symmetry axes in a given geometry, while the characteristic length range of 3–6  $\mu\text{m}$  further restricts the choice among these axes (Fig. 4a,b,d). This range is defined by the lengths to which Min proteins can scale their concentration gradients. Notably, 3–6  $\mu\text{m}$  coincides with the lengths of wild-type *E. coli* cells undergoing cytokinesis, indicating an evolved optimality of Min system in adaptation to the size of *E. coli*. As it is essential for the binary fission process to distribute the cellular material equally to its progeny, the sensing of both symmetry and scale by the Min proteins are indispensable for their role as a spatial regulator for cell division. The diverse patterns uncovered in our study provide valuable insight on how Min homologues adapt to bacteria with diverse morphologies and modes of division<sup>41,42</sup>. For example, the transversal mode may well be orchestrated by Min homologues found in  $\gamma$ -proteobacterial symbionts that divide along their long axis<sup>41</sup>.

Our numerical simulations revealed that the symmetry selection and characteristic length range both derive from the self-activation/inhibition kinetics responsible for the oscillatory dynamics of Min proteins in the three-dimensional confinement of a cell. This type

of microscopic interaction has been found to underlie a broad spectrum of Turing reaction-diffusion patterns, including intracellular polar protein networks and actin waves in eukaryotic cells<sup>5,43,44</sup>, suggesting that the ability to sense global features of biological boundaries may be intrinsic to many spatial patterns in cells.

The bacterial cell sculpting reported here reveals that spatial boundaries can facilitate simple molecular interactions and result in far more versatile functions than previously understood. We expect that it can also be applied to unravel the fundamental mechanisms of intracellular spatial organization, including protein/RNA/lipid localization, cytoskeletal dynamics and chromosome organization<sup>45</sup>.

## Methods

Methods and any associated references are available in the [online version of the paper](#).

Received 3 November 2014; accepted 19 May 2015;

published online 22 June 2015; corrected online 25 June 2015

## References

1. Turing, A. M. The chemical basis of morphogenesis. *Phil. Trans. R. Soc. Lond. B* **237**, 37–72 (1952).
2. Gierer, A. & Meinhardt, H. A theory of biological pattern formation. *Kybernetik* **12**, 30–39 (1972).
3. Meinhardt, H. & de Boer, P. A. J. Pattern formation in *Escherichia coli*: a model for the pole-to-pole oscillations of Min proteins and the localization of the division site. *Proc. Natl Acad. Sci. USA* **98**, 14202–14207 (2001).
4. Huang, K. C., Meir, Y. & Wingreen, N. S. Dynamic structures in *Escherichia coli*: spontaneous formation of MinE rings and MinD polar zones. *Proc. Natl Acad. Sci. USA* **100**, 12724–12728 (2003).
5. Goryachev, A. B. & Pokhilko, A. V. Dynamics of Cdc42 network embodies a Turing-type mechanism of yeast cell polarity. *FEBS Lett.* **582**, 1437–1443 (2008).
6. Kondo, S. & Miura, T. Reaction-diffusion model as a framework for understanding biological pattern formation. *Science* **329**, 1616–1620 (2010).
7. Halatek, J. & Frey, E. Highly canalized MinD transfer and MinE sequestration explain the rigidity of robust MinCDE-protein dynamics. *Cell Rep.* **1**, 741–752 (2012).
8. Noorduyn, W. L., Grinthal, A., Mahadevan, L. & Aizenberg, J. Rationally designed complex, hierarchical microarchitectures. *Science* **340**, 832–837 (2013).
9. Moseley, J. B. & Nurse, P. Cell division intersects with cell geometry. *Cell* **142**, 184–188 (2010).
10. Raskin, D. M. & de Boer, P. A. J. Rapid pole-to-pole oscillation of a protein required for directing division to the middle of *Escherichia coli*. *Proc. Natl Acad. Sci. USA* **96**, 4971–4976 (1999).
11. Hu, Z. & Lutkenhaus, J. Topological regulation of cell division in *Escherichia coli* involves rapid pole to pole oscillation of the division inhibitor MinC under the control of MinD and MinE. *Mol. Microbiol.* **34**, 82–90 (1999).
12. Ben-Jacob, E. Bacterial self-organization: co-enhancement of complexification and adaptability in a dynamic environment. *Phil. Trans. R. Soc. Lond. A* **361**, 1283–1312 (2003).
13. Männik, J. et al. Robustness and accuracy of cell division in *Escherichia coli* in diverse cell shapes. *Proc. Natl Acad. Sci. USA* **109**, 6957–6962 (2012).
14. Young, K. D. The selective value of bacterial shape. *Microbiol. Mol. Biol. Rev.* **70**, 660–703 (2006).
15. Hu, Z. & Lutkenhaus, J. Topological regulation of cell division in *E. coli*: spatiotemporal oscillation of MinD requires stimulation of its ATPase by MinE and phospholipid. *Mol. Cell* **7**, 1337–1343 (2001).
16. Lackner, L. L., Raskin, D. M. & de Boer, P. A. J. ATP-dependent interactions between *Escherichia coli* Min proteins and the phospholipid membrane *in vitro*. *J. Bacteriol.* **185**, 735–749 (2003).
17. Loose, M., Fischer-Friedrich, E., Ries, J., Kruse, K. & Schwillie, P. Spatial regulators for bacterial cell division self-organize into surface waves *in vitro*. *Science* **320**, 789–792 (2008).
18. Ivanov, V. & Mizuuchi, K. Multiple modes of interconverting dynamic pattern formation by bacterial cell division proteins. *Proc. Natl Acad. Sci. USA* **107**, 8071–8078 (2010).
19. Schweizer, J. et al. Geometry sensing by self-organized protein patterns. *Proc. Natl Acad. Sci. USA* **109**, 15283–15288 (2012).
20. Zieske, K. & Schwillie, P. Reconstitution of self-organizing protein gradients as spatial cues in cell-free systems. *eLife* **3**, e03949 (2014).
21. Vecchiarelli, A. G., Li, M., Mizuuchi, M. & Mizuuchi, K. Differential affinities of MinD and MinE to anionic phospholipid influence Min patterning dynamics *in vitro*. *Mol. Microbiol.* **93**, 453–463 (2014).
22. Corbin, B. D., Yu, X.-C. & Margolin, W. Exploring intracellular space: function of the Min system in round-shaped *Escherichia coli*. *EMBO J.* **21**, 1998–2008 (2002).

23. Varma, A., Huang, K. C. & Young, K. D. The Min system as a general cell geometry detection mechanism: branch lengths in Y-shaped *Escherichia coli* cells affect Min oscillation patterns and division dynamics. *J. Bacteriol.* **190**, 2106–2117 (2008).
24. Renner, L. D. & Weibel, D. B. Cardiolipin microdomains localize to negatively curved regions of *Escherichia coli* membranes. *Proc. Natl Acad. Sci. USA* **108**, 6264–6269 (2011).
25. Tzypas, A., Banzhaf, M., Gross, C. A. & Vollmer, W. From the regulation of peptidoglycan synthesis to bacterial growth and morphology. *Nature Rev. Microbiol.* **10**, 123–136 (2012).
26. Takeuchi, S., DiLuzio, W. R., Weibel, D. B. & Whitesides, G. M. Controlling the shape of filamentous cells of *Escherichia coli*. *Nano Lett.* **5**, 1819–1823 (2005).
27. Männik, J., Driessen, R., Galajda, P., Keymer, J. E. & Dekker, C. Bacterial growth and motility in sub-micron constrictions. *Proc. Natl Acad. Sci. USA* **106**, 14861–14866 (2009).
28. Cabeen, M. T. *et al.* Bacterial cell curvature through mechanical control of cell growth. *EMBO J.* **28**, 1208–1219 (2009).
29. Fischer-Friedrich, E., Meacci, G., Lutkenhaus, J., Chaté, H. & Kruse, K. Intra- and intercellular fluctuations in Min-protein dynamics decrease with cell length. *Proc. Natl Acad. Sci. USA* **107**, 6134–6139 (2010).
30. Shannon, C. E. A mathematical theory of communication. *Bell Syst. Tech. J.* **27**, 379–423 (1948).
31. Yu, X.-C. & Margolin, W. FtsZ ring clusters in min and partition mutants: role of both the Min system and the nucleoid in regulating FtsZ ring localization. *Mol. Microbiol.* **32**, 315–326 (1999).
32. Fange, D. & Elf, J. Noise-induced Min phenotypes in *E. coli*. *PLoS Comput. Biol.* **2**, e80 (2006).
33. Ben-Zvi, D., Shilo, B.-Z., Fainsod, A. & Barkai, N. Scaling of the BMP activation gradient in *Xenopus* embryos. *Nature* **453**, 1205–1211 (2008).
34. Ben-Zvi, D. & Barkai, N. Scaling of morphogen gradients by an expansion-repression integral feedback control. *Proc. Natl Acad. Sci. USA* **107**, 6924–6929 (2010).
35. Lauschke, V. M., Tsiarris, C. D., Francois, P. & Aulehla, A. Scaling of embryonic patterning based on phase-gradient encoding. *Nature* **493**, 101–105 (2013).
36. Averbukh, I., Ben-Zvi, D., Mishra, S. & Barkai, N. Scaling morphogen gradients during tissue growth by a cell division rule. *Development* **141**, 2150–2156 (2014).
37. Loose, M., Fischer-Friedrich, E., Herold, C., Kruse, K. & Schwiller, P. Min protein patterns emerge from rapid rebinding and membrane interaction of MinE. *Nature Struct. Mol. Biol.* **18**, 577–583 (2011).
38. Hoffmann, M. & Schwarz, U. S. Oscillations of Min-proteins in micropatterned environments: a three-dimensional particle-based stochastic simulation approach. *Soft Matter* **10**, 2388–2396 (2014).
39. Hsieh, C.-W. *et al.* Direct MinE–membrane interaction contributes to the proper localization of MinDE in *E. coli*. *Mol. Microbiol.* **75**, 499–512 (2010).
40. Park, K.-T. *et al.* The Min oscillator uses MinD-dependent conformational changes in MinE to spatially regulate cytokinesis. *Cell* **146**, 396–407 (2011).
41. Leisch, N. *et al.* Growth in width and FtsZ ring longitudinal positioning in a gammaproteobacterial symbiont. *Curr. Biol.* **22**, R831–R832 (2012).
42. Pende, N. *et al.* Size-independent symmetric division in extraordinarily long cells. *Nature Commun.* **5**, 4803 (2014).
43. Vicker, M. G. F-actin assembly in *Dictyostelium* cell locomotion and shape oscillations propagates as a self-organized reaction-diffusion wave. *FEBS Lett.* **510**, 5–9 (2002).
44. Chau, A. H., Walter, J. M., Gerardin, J., Tang, C. & Lim, W. A. Designing synthetic regulatory networks capable of self-organizing cell polarization. *Cell* **151**, 320–332 (2012).
45. Shapiro, L., McAdams, H. H. & Losick, R. Why and how bacteria localize proteins. *Science* **326**, 1225–1228 (2009).

### Acknowledgements

The authors thank E. van Rijn, D. de Graaff, W. Postek, J. van der Does, J. Kerssenmakers and Z. Huang for technical assistance, Y. Caspi, Y.-L. Shih, A. Lindert, L. Rothfield, A. Meyer and C. Plesa for materials, E. Frey and J. Halatek for discussions on their model, C. Danelon and F. Hol for discussions, and the CSHL Computational Cell Biology Summer School and VirtualCell (NIH grant P41-GM103313). This work was partly supported by the Netherlands Organisation for Scientific Research (NWO/OCW) as part of the Frontiers of Nanoscience programme, NanoNextNL programme 3B (F.W.) and European Research Council NanoforBio no. 247072 (C.D.).

### Author contributions

F.W., J.E.K. and C.D. conceived the experiments, discussed the work and wrote the paper. F.W. and B.v.S performed the experiments. F.W. analysed the data, derived the mechanisms and carried out computer simulations.

### Additional information

Supplementary information is available in the [online version](#) of the paper. Reprints and permissions information is available online at [www.nature.com/reprints](http://www.nature.com/reprints). Correspondence and requests for materials should be addressed to C.D.

### Competing financial interests

The authors declare no competing financial interests.

## Methods

**Mask nanofabrication.** A silicon wafer (universitywafer.com) was spin-coated with resist NEB-22 (Sumitomo Chemical)<sup>46</sup>. Pre-designed features were patterned through an electron-beam lithography system (Leica EBPG 5000+) with a beam step size of 20 nm. The exposed resist was removed by solvent Microposit MF-322 solution (Rohm and Haas) and the exposed wafer surface was etched using an AMS Bosch Etcher. The remaining resist was removed using oxygen plasma.

**PDMS microchamber patterning.** The patterned silicon wafer was silanized by tridecafluoro-1,1,2,2-tetrahydrocyclohexylchloro-silane (97%, ABCR), and used as a mold for creating microchambers. A 5- $\mu\text{l}$  mixture of Sylgard elastomer 184 (base-to-curing agent ratio 5:1) was applied onto the microstructures of the silicon surface and subsequently covered with a clean microscope coverglass (thickness 0.13–0.17  $\mu\text{m}$ ) to spread the mixture throughout the area of the glass. The wafer attached to the coverglass was baked in an oven at 70 °C for 3 hours until the solvent was fully evaporated, which resulted in a  $\sim 10\text{-}\mu\text{m}$ -thick layer of polydimethylsiloxane (PDMS) between the coverglass and the silicon substrate. The coverglass with the patterned PDMS layer was subsequently recovered from the silicon wafer. For inspection under a scanning electron microscope (Phillips XL 30), the resulting silicon mold and PDMS structures were deposited with 10-nm-thick gold using a Temescal deposition system.

**Cell-sculpting technique.** An *E. coli* bacterial culture incubated overnight at 30 °C was back-diluted to OD<sub>600</sub> = 0.02 in fresh M9 medium supplemented with 4  $\mu\text{M}$  A22 (Merk Chemicals), and incubated for 3.5 hours at 30 °C. 1  $\mu\text{l}$  of the bacterial culture was then pipetted onto the PDMS chambers on a coverglass that was clamped onto a custom-made baseplate. The droplet was then immediately covered by a 4.8% agarose pad containing M9 broth, 0.4% glucose, 0.25% protein hydrolysate ampicase, 4  $\mu\text{M}$  A22 and 25  $\mu\text{g ml}^{-1}$  cephalixin (Sigma-Aldrich). A thin piece of tissue wetted with water was placed above the device to keep the humidity at a high level, and a piece of stretched parafilm was used to enclose the device to prevent drying but allow air exchange. The base-plate was subsequently mounted onto the microscope stage and incubated at 26 °C during the course of the experiments.

**Fluorescence imaging.** Fluorescence imaging was carried out using Nikon Ti-E microscope with CFI Apo TIRF objective with an NA of 1.49. The microscope was enclosed by a custom-made chamber that was pre-heated overnight and kept at 26–27 °C. For excitation of sfGFP or NirFP signal, cells were illuminated by a Nikon-Intensilight illumination lamp through a GFP filter cube ( $\lambda_{\text{ex}}/\lambda_{\text{bs}}/\lambda_{\text{em}} = 450\text{--}490/495/500\text{--}550\text{ nm}$ ) or a RFP filter cube ( $\lambda_{\text{ex}}/\lambda_{\text{bs}}/\lambda_{\text{em}} = 540\text{--}580/585/592\text{--}668$ ). The fluorescence signal was recorded by an Andor iXon EMCCD camera. The MinD dynamics were imaged with a frame time-interval of 5 s for 25 frames.

**Bacterial strain construction and characterization.** Bacterial strains were constructed via  $\lambda$ Red recombination<sup>47,48</sup> and P1 phage transduction. All primers, strains and plasmids used in this study are listed in Supplementary Tables 2 and 3. Protein expression levels are characterized through western blot analysis using MinD and FtsZ antibodies. For more details please see Supplementary Information.

**Image analysis.** Analysis of fluorescent microscopy images was carried out using Matlab. For more details please see Supplementary Information.

**Shape selection and data binning.** All rectangular and square-shaped cells were selected for data analysis using the following criteria: (1) cell area covering more than 90% of the smallest rectangle that the cell shape can fit in, and (2) diagonal lines having a length difference smaller than 5%. Cell widths and lengths were binned to 0.50  $\mu\text{m}$  (for example,  $4.00 \pm 0.25\ \mu\text{m}$ ) for statistical analysis unless specified otherwise. Additional criteria for square shapes are: (1) an aspect ratio smaller than 1.05, and (2) a difference between measured length and width smaller than the diffraction limit of around 0.25  $\mu\text{m}$ . For statistics on square shapes, the denoted sizes are the average length of the sides. Larger cell sizes—that is, with a width or length above 4.75  $\mu\text{m}$ —are binned to 1.0  $\mu\text{m}$ , as shown in the phase diagrams (Fig. 3d).

Note that due to the multi-fold symmetry of the square shape, all square-shape cells were rotated or reflected to show side-to-side oscillations horizontally, and diagonal oscillations no bigger than +45° with respect to the horizontal axis. Thus, for analyses on the Min patterns in the square shapes, the oscillation angles are set to values between 0° and 45°. However, for consistency in comparison to the 7 modes of the oscillations in rectangular shapes (in Fig. 3), the side-to-side mode was grouped into longitudinal and transversal modes according to the quantified small length–width difference in square shapes. Hence, for example, in the case of  $3.00 \pm 0.25\ \mu\text{m}$  squares, whereas the fraction of side-to-side mode is higher than the fraction of the diagonal mode (Fig. 2b), the diagonal mode seems to occur more frequently than the individual fraction of either longitudinal mode or transversal mode (Fig. 3d).

**Numerical simulations.** The detailed set of interactions between MinD, MinE, ATP and the cytoplasmic membrane, and the set of reaction-diffusion equations are listed in Supplementary Methods. The reaction kinetic parameters used to reproduce symmetry selection, gradient scaling, and all the major patterns are listed in Supplementary Table 4. The MinD/MinE concentration ratio and diffusion rates are set to be identical with the simulations in the Halatek–Frey model<sup>7</sup>, where the choices of these values are explained. Based on the set of interactions and kinetic parameters, a reaction diagram was constructed between a cytosolic compartment and the cytoplasmic membrane in the software VirtualCell<sup>49</sup>. Three-dimensional compartments were constructed and latticed with a grid spacing of  $dx = dy = dz = 0.08\ \mu\text{m}$ . The height of all objects was fixed to be  $z = 1.00\ \mu\text{m}$ . For more details please see Supplementary Information.

## References

- Huang, Z., Pedaci, F., van Oene, M., Wiggin, M. J. & Dekker, N. H. Electron beam fabrication of birefringent microcylinders. *ACS Nano* **5**, 1418–1427 (2011).
- Datsenko, K. A. & Wanner, B. L. One-step inactivation of chromosomal genes in *Escherichia coli* K-12 using PCR products. *Proc. Natl Acad. Sci. USA* **97**, 6640–6645 (2000).
- Wu, F., van Rijn, E., van Schie, B. G. C., Keymer, J. E. & Dekker, C. Multicolor imaging of bacterial nucleoid and division proteins with blue, orange and near-infrared fluorescent proteins. *Front. Microbiol.* **6**, 607 (2015).
- Loew, L. M. & Schaff, J. C. The virtual cell: a software environment for computational cell biology. *Trends Biotechnol.* **19**, 401–406 (2001).

## Erratum: Symmetry and scale orient Min protein patterns in shaped bacterial sculptures

Fabai Wu, Bas G. C. van Schie, Juan E. Keymer and Cees Dekker

*Nature Nanotechnology* <http://dx.doi.org/10.1038/nnano.2015.126> (2015); published online 22 June 2015; corrected online 25 June 2015.

In the version of this Article previously published online the Methods section was inadvertently omitted. This has been corrected for all versions of the Article.